*Korean J. Chem. Eng.*, 39(12), 3227-3245 (2022)
DOI: 10.1007/s11814-022-1267-0

pISSN: 0256-1115
eISSN: 1975-7220

# Numerical investigation and deep learning-based prediction of heat transfer characteristics and bubble dynamics of subcooled flow boiling in a vertical tube

**Erfan Eskandari*, Hasan Alimoradi**, Mahdi Pourbagian*,†, and Mehrzad Shams****

*Computational and Data-Driven Multiphysics Laboratory, Faculty of Mechanical Engineering, K.N. Toosi University of Technology, Tehran, Iran
**Multiphase Flow Lab, Faculty of Mechanical Engineering, K.N. Toosi University of Technology, Tehran, Iran
(*Received 21 April 2022 • Revised 9 August 2022 • Accepted 18 August 2022*)

**Abstract**−Subcooled flow boiling presents an enormous ability of heat transfer rate, which is extremely important in the heat-dissipating systems of many industrial applications, such as power plants and internal combustion engines. Using an Euler-Euler-based three-dimensional numerical simulation of subcooled flow boiling in a vertical tube, we investigated different heat transfer quantities (average and local heat transfer coefficient, average and local vapor volume fraction, average and local wall temperature) and bubble dynamics quantities (bubble departure diameter, bubble detachment frequency, bubble detachment waiting time, and nucleation site density) under various boundary conditions (pressure, subcooled temperature, mass flux, heat flux). Numerical results show that an increase in heat flux leads to the increase in all of the physical quantities of interest but the bubble detachment frequency. An entirely opposite behavior is observed when we change the mass flux and inlet subcooled temperature. Furthermore, a rise in pressure reduces all of the target quantities but the wall temperature and bubble detachment frequency. Since numerical simulation of such multiphase flow requires significant computational resources, we also present a deep learning approach, based on artificial neural networks (ANN), to predicting the physical quantities of interest. Prediction results demonstrate that the ANN model is capable of accurately predicting the target quantities with mean absolute errors less than 2.5% and R-squared more than 0.93.

Keywords: Subcooled Flow Boiling, Numerical Simulation, Bubble Dynamics, Artificial Neural Networks, Deep Learning

## INTRODUCTION

Recently, the requirement for higher amounts of heat dissipation in various industrial applications has led to the usage of subcooled flow boiling in tubes. Therefore, there is a vast body of studies investigating the benefits and applications of flow boiling in tubes as an effective cooling mechanism that can dissipate large amounts of heat. The primary advantage of flow boiling is the capability of this process in dissipation of a significant amount of thermal power as it exploits the fluid latent heat. The effective life of equipment can also be elongated due to small temperature differences in flow boiling. Furthermore, since the fluid undergoes a phase-change process, the required inlet velocity is much lower than that of single-phase flows [1].

A conventional phase change technique in cooling systems is nucleate boiling heat transfer, which is well-known for its powerful heat dissipation ability. The biggest concern in this process is burnout, which happens when the wall temperature gets higher than the material's melting point. Many studies have addressed this issue [2-7]. Subcooled flow boiling is a particular type of nucleate boiling in which the bulk temperature is below the saturation temperature of the working fluid. The subcooled flow boiling in channels with relatively small diameters has gained attention due to its simplicity to use and its high surface-to-volume ratio. In subcooled flow boiling, prior to the boiling process, the fluid temperature is augmented by convection heat transfer. Then the layer adjacent to the wall experiences subcooled nucleate boiling. Later, the smaller bubbles leaving nucleation sites merge to form a bigger bubble. This process continues until the flow pattern transforms to slug flow.

Numerous experimental and numerical studies have been conducted to investigate subcooled flow boiling. Before the advent of high-performance computing devices, researchers employed empirical approaches to investigate flow boiling processes [8,9]. Because of the complex physical behavior of boiling processes, these experiments were conducted over a small range of effective parameters. Despite these restrictions, empirical correlations were proposed [10, 11]. To improve the pioneers' work, Chen [12] proposed a method in which two effective parameters, i.e., two-phase Reynolds number and bubble dynamics function, are superimposed which led to an average deviation of ±12% among 600 data points. Chen's correlation is valid for vapor volume fractions less than 0.7. Shah [13] utilized dimensionless numbers including Froude number, boiling number, and convection number to fully capture the behavior of saturated flow boiling. His graphical model was based on 780 data points of eight working fluids covering a wide variety of pressures, and had a mean deviation of 14%. Bennet and Chen [14] presented a modified model of Chen's correlation by adding the Prandtl number. They carried out an experiment on pure fluids and mixtures and reported over 1,000 data points and compared these data points with their proposed correlation which led to a mean devia-

†To whom correspondence should be addressed.
E-mail: pourbagian@kntu.ac.ir
Copyright by The Korean Institute of Chemical Engineers.

tion of 14.9%. Kandlikar [15] developed a correlation to predict saturated flow boiling heat transfer coefficient. His model was comprised of two components, i.e., nucleate boiling and convective boiling, each contributing to the overall heat transfer coefficient. This model was examined with 5,246 data points and was verified for water and R-113 with a mean deviation of 15.9% and 18.8%, respectively. Lee and Lee [16] studied a channel with the working fluid of R-113. They observed the effects of a variety of parameters on heat transfer coefficient. Alimoradi et al. [17] presented a numerical study on the effects of vibration on pool boiling. They found the increase in vibration leads to improvements in heat transfer coefficient. Also, Zaboli et al. [18] studied the effects of heat flux and nanofluid concentration on nanofluid pool boiling. They concluded that in high heat fluxes the dependency on nanoparticle concentration increases. Recently, Bertsch [19] formulated a semi-empirical correlation based on Chen's model. Since Chen's model and its modifications [14,20,21] are valid for conventional tubes, Bertsch suggested a new model for smaller channels. A 3,899 dataset improved the previous models and achieved the mean absolute error of less than 30%. Fang's correlation [22] shows a tremendous increase in the number of data points and is formulated based on 17,778 data points; later, it is validated by a second dataset of 6,664 points. This model utilizes a group of dimensionless numbers including boiling number, Froude number, and Bond number. The reported results indicate the mean absolute deviation of 4.5% and 4.4% for the first and second datasets. Piasecka [23] carried out an experiment to examine subcooled flow boiling in a rectangular mini-channel containing seven different orientations at reasonably low pressures up to 400 kPa. Later, Strąk and Piasecka [24] used the same dataset to compare the applicability of the correlations and then formulated a new one for subcooled flow boiling. Their model was able to achieve a mean absolute percentage error of 14% in predicting the Nusselt number. Paul et al. [25] examined a convective flow boiling regime and indicated that the vapor Reynolds number is overlooked in the previous studies. Not only did they show that the effect of liquid Reynolds number in high qualities is negligible, but they also added an enhancement factor representing Reynolds number for vapor phase. Interestingly, the results illustrate that using Reynolds number in the vapor phase at low heat flux and pressure is quite considerable. Moreover, it was concluded that the vapor Reynolds number substantially affects in high qualities.

Experimental and numerical methods require significant financial and computational resources [26-29]. Soft computing techniques, such as fuzzy logic, genetic algorithms, artificial neural networks (ANNs), and machine learning are promising methods by which a plethora of engineering problems can be solved with less amount of resources. Among all the techniques, ANNs are more common in engineering problems for two main reasons; first, the implementation of the algorithms is very straightforward, and second, there is no need to find the direct relation between the input and output parameters. This is mainly advantageous in problems like two-phase flows which possess a complex behavior, and hence many parameters seem to be contributing to the flow pattern [30, 31]. Many recent studies have utilized ANNs in thermal analysis problems. Alimoradi and Shams [32] used a genetic algorithm and an artificial neural network in a subcooled flow boiling to optimize the highest temperature at the wall and void fraction at the outlet of a pipe. An experimental dataset consisting of 350 data points in a horizontal pipe was used to predict two parameters for different flow patterns using a deep neural network by Seong et al. [33]. Their network managed to predict liquid holdup and pressure gradient with a mean absolute percentage error of 8.08% and 23.76%, respectively.

Although there are numerous research activities [34,35] on the utilization of ANNs in two-phase flow, there is no study covering both average and local thermal characteristics of subcooled flow boiling along with the bubble dynamics. In the present work, we addressed this gap by generating a large dataset consisting of more than 400 three-dimensional numerical simulations of subcooled flow boiling over a wide range of operating conditions with various pressures, heat fluxes, mass fluxes and subcooled temperatures, and then employing ANNs to accurately predict the average and local quantities of interest. To reduce the errors of the predictive model, a comprehensive hyperparameter tuning was performed and the best model was selected. The model can be used to investigate heat transfer characteristics and bubble dynamics of subcooled flow boiling with any set of operating conditions at any location inside the tube. This can be very useful in terms of cost reduction both computationally and experimentally.

## NUMERICAL APPROACH

We utilize the Eulerian two-phase model, in which the liquid water and vapor are considered as continuous and dispersed flow. In the Eulerian model, the conservation equations are separately solved for each phase. Moreover, the inter-phase forces are taken into account by adding the inter-phase mass transfer terms. In the Euler-Euler model, both phases are described on a globally fixed coordinate system. That is, the particles-in our case the bubbles-are not tracked in space and time. Instead, the distribution of particle phase properties is considered. In this model, an additional transport equation is added for volume fraction, which is later studied in the present work.

### 1. Governing Equations

As mentioned earlier, the proposed CFD modeling uses the Eulerian multiphase model (EMM) with the addition of heat transfer correlations and source terms in the conservation equations, which are solved for each phase. The continuity equations for liquid and vapor phases [36] read:

$$\frac{\partial(\rho_l \alpha_l)}{\partial \mathrm{t}} + \nabla \cdot (\rho_l \alpha_l \mathbf{u}_l) = \Gamma_{lg} \tag{1}$$

$$\frac{\partial(\rho_g \alpha_g \mathrm{f}_i)}{\partial \mathrm{t}} + \nabla \cdot (\rho_g \alpha_g \mathbf{u}_g) = \mathrm{S}_i - \mathrm{f}_i \Gamma_{lg} \tag{2}$$

where, $\rho_l$, $\rho_g$, $\alpha_l$, $\alpha_g$, $\mathrm{u}_l$, and $\mathrm{u}_g$ are liquid density, vapor density, liquid volume fraction, vapor volume fraction, liquid velocity, and vapor velocity, respectively. Additionally, $\mathrm{S}_i$ is a source term for the formation and break-up of the bubbles in the population balance model for the vapor phase, and $\mathrm{f}_i$ is a scalar fraction related to the density of the bubble classes. The momentum equations for both

phases are given by:

$$\frac{\partial(\rho_l\alpha_l\mathbf{u}_l)}{\partial t}+\nabla\cdot(\rho_l\alpha_l\mathbf{u}_l\mathbf{u}_l)=-\alpha_l\nabla P+\alpha_l\rho_l\mathbf{g}+\nabla[\alpha_l\mu_l^e(\nabla\mathbf{u}_l+(\nabla\mathbf{u}_l)^T)]+(\Gamma_{lg}\mathbf{u}_g-\Gamma_{gl}\mathbf{u}_g)+F_{lg} \quad (3)$$

$$\frac{\partial(\rho_g\alpha_g\mathbf{u}_g)}{\partial t}+\nabla\cdot(\rho_g\alpha_g\mathbf{u}_g\mathbf{u}_g)=-\alpha_g\nabla P+\alpha_g\rho_g g+\nabla[\alpha_g\mu_g^e(\nabla\mathbf{u}_g+(\nabla\mathbf{u}_g)^T)]+(\Gamma_{gl}\mathbf{u}_l-\Gamma_{lg}\mathbf{u}_g)+F_{gl} \quad (4)$$

where, $F_{lg}$ and $F_{gl}$ are the forces exerted to each phase. The correlation between these two forces is $F_{lg}=-F_{gl}$. The mass transfer rate $\Gamma_{lg}$ is mainly due to distillation, and $\Gamma_{gl}$ is the vapor generation rate. To be more precise, $\Gamma_{gl}$ is the total mass of the bubbles that get separated from the heating surface. The energy equations for both phases read:

$$\frac{\partial(\rho_l\alpha_l H_l)}{\partial t}+\nabla\cdot(\rho_l\alpha_l\mathbf{u}_l H_l)=\nabla[\alpha_l k_l^e(\nabla T_l)]+(\Gamma_{gl}H_l-\Gamma_{lg}H_g) \quad (5)$$

$$\frac{\partial(\rho_g\alpha_g H_g)}{\partial t}+\nabla\cdot(\rho_g\alpha_g\mathbf{u}_g H_g)=\nabla[\alpha_g k_g^e(\nabla T_g)]+(\Gamma_{lg}H_g-\Gamma_{gl}H_l) \quad (6)$$

where, $\mu_l$, $\mu_g$, $H_l$, $H_g$, $k_l$, and $k_g$ are the liquid dynamic viscosity, vapor dynamic viscosity liquid enthalpy, vapor enthalpy, liquid heat conductivity coefficient, and vapor heat conductivity coefficient, respectively.

Mass transfer parameters are calculated by:

$$\Gamma_{lg}=\frac{h a_{if} T_{sub}}{h_{fg}} \quad (7)$$

$$\Gamma_{gl}=\frac{Q_e}{h_{fg}} \quad (8)$$

The k-$\varepsilon$ turbulence model [37] is utilized for the simulation of Reynolds stresses that appeared in the averaged Navier Stokes equations. This method is basically comprised of two equations to address the eddy viscosity. The standard k-$\varepsilon$ model is presented as:

$$\nabla\cdot(\rho_{eff}kU)=\nabla\cdot\left[\left(\mu_{eff}+\frac{\mu_t}{\sigma_k}\right)(\nabla k)\right]+G_k-\rho_{eff}\varepsilon \quad (9)$$

$$\nabla\cdot(\rho_{eff}\varepsilon U)=\nabla\cdot\left[\left(\mu_{eff}+\frac{\mu_t}{\sigma_\varepsilon}\right)(\nabla\varepsilon)\right]+C_{1\varepsilon}\frac{\varepsilon}{k}G_k-C_{2\varepsilon}\rho_{eff}\frac{\varepsilon^2}{k} \quad (10)$$

Where,

$$G_k=-\rho_{eff}\overline{u_i'u_j'}(\nabla U) \quad (11)$$

$$\mu_t=\rho_{eff}C_\mu\frac{k^2}{\varepsilon} \quad (12)$$

In these equations, $C_\mu$=0.09, $\sigma_k$=1.00, $\sigma_\varepsilon$=1.30, $C_{1\varepsilon}$=1.44, and $C_{2\varepsilon}$=1.92. Also, k and $\varepsilon$ are turbulence kinetic energy and dissipation rate of turbulence kinetic energy, respectively. $u_i'$, $u_j'$, and U are the fluctuating component of velocity in x direction, y direction and the velocity field, respectively.

The Ranz and Marshal model [38] is used to calculate the heat transfer coefficient in the liquid phase. The drag force between the two phases is measured by the Ishii-Zuber model [39].

## 2. The Heat Flux Partitioning Model

Kurul and Podowski's model [40] is used to determine the heat flux transferred to the fluid. According to their model, the heat flux from the heater surface is transferred to the fluid through three mechanisms--evaporation, quenching, and convection:

$$q=q_e+q_q+q_c \quad (13)$$

Each of these components is formulated as follows:

$$q_e=\frac{\pi}{6}d_w^3\rho_g f n_a h_{fg} \quad (14)$$

$$q_q=\frac{2}{\sqrt{\pi}}fA_q\sqrt{t_w\lambda_l\rho_l c_{p,l}}(T_w-T_l) \quad (15)$$

$$q_c=A_c St\rho_l c_{p,l}u_l(T_w-T_l) \quad (16)$$

where, $d_w$, f, $n_a$, $t_w$, $A_c$, and $A_q$ are bubble departure diameter, bubble departure frequency, active site density, bubble waiting time, and the area of fraction of the heater surface subjected to convection and quenching, respectively. Due to the inherent complexity of bubble dynamics, these parameters are generally formulated empirically.

The active nucleation site density is determined by Lemmert and Chawala's model [41]:

$$n_a=(185T_{sup})^{1.805} \quad (17)$$

where, $T_{sup}$ is the wall super heat which is equivalent to $T_{sup}=T_w-T_{sat}$. Bubble departure diameter is calculated by the Tolubinsky and Kostanchuk correlation [42]:

$$d_w=\min\left(0.6\exp\left(\frac{-\Delta T_{sub,Lw}}{45}\right),\ 1.4\right) \quad (18)$$

where, $\Delta T_{sub,Lw}$ is the liquid subcooling temperature. Cole's correlation [43] is employed to compute the bubble departure frequency:

$$f=\sqrt{\frac{4g(\rho_l-\rho_g)}{3d_w\rho_l}} \quad (19)$$

Finally, the waiting time of the bubble, which is the interval between the departure and the appearance of a bubble at the same nucleation site, is calculated by the Kurul and Podowski's model [40]:

$$t_w=\frac{0.8}{f} \quad (20)$$

## 3. Geometry and Boundary Conditions

Fig. 1 shows the schematic geometry of the present problem. Water is pumped into the pipe of 2-meter length and a diameter of 15.4 mm with a specific inlet velocity or mass flux and a specific subcooled temperature. The pipe is uniformly heated with a constant heat flux, which experimentally is more tangible compared to the constant temperature boundary condition. The no-slip condition is applied on the walls. In addition, the bubble formation of the boiling process is presented. Over 400 numerical cases were three-dimensionally simulated, and the results were compared in the following. The inlet boundary condition is based on a given subcooled temperature and velocity. Since the cross-section of the geometry is circular, a uniform heat flux was applied throughout the pipe length. The outlet boundary condition is based on the atmospheric pressure. Also, the no slip boundary condition is applied on

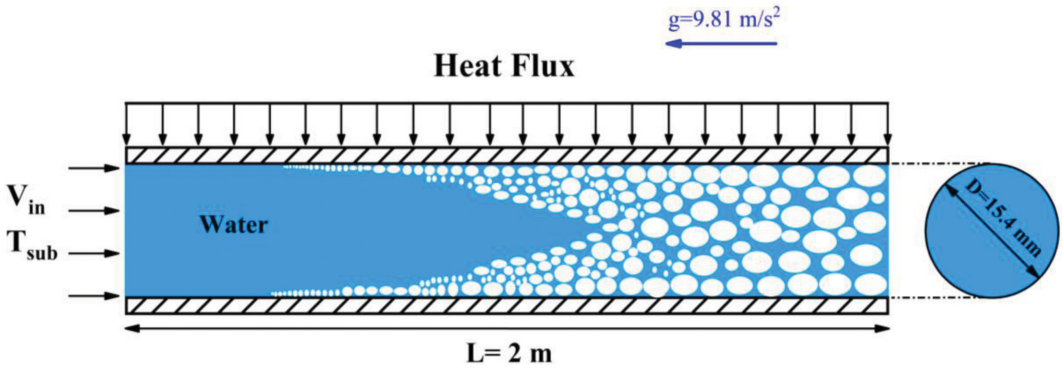



**Fig. 1. Schematic geometry of the present problem.**

**Table 1. The selected data points for validation of the numerical simulations**

| Validation case | Pressure (MPa) | Mass flux (kg/m²s) | Heat flux (kW/m²) | Subcooled temperature (K) | Section/ Diameter (cm) |
|---|---|---|---|---|---|
| (1) [44] | 4.5 | 900 | 570 | 58.2 | Diameter=1.54 |
| (2) [45] | 5.512 | 906 | 496.5 | 12.5 | 0.261×2.54 |
| (3) [45] | 6.89 | 877.5 | 496.5 | 12.1 | 0.261×2.54 |

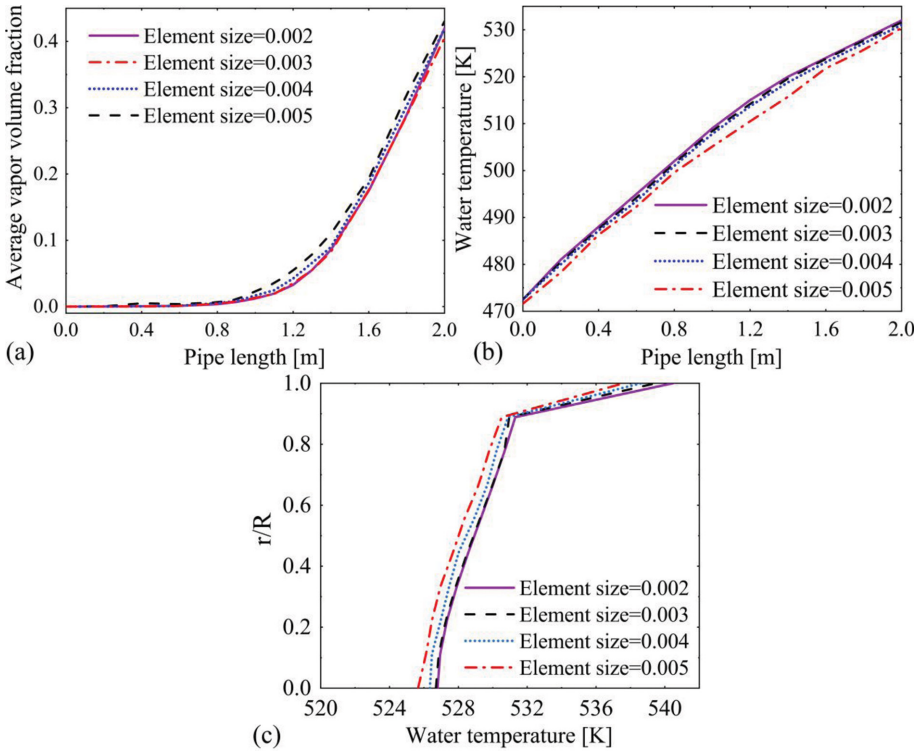



**Fig. 2. Comparison of (a) average vapor volume fraction along the pipe, (b) average water temperature along the pipe, and (c) average water temperature along the radius of the pipe with different element sizes.**

the tube surface.

## 4. Grid Independency and Validation

To validate the numerical data in the present study, the experimental data of Bartolomoi et al. [44] and Rouhani and Axelsson [45] are used. The selected data points for validation is provided in Table 1.

To conduct a grid independence study, the average vapor volume fraction and water temperature along the pipe length are obtained using different element sizes, and the results are shown in Fig. 2(a) and Fig. 2(b). The results of different element sizes for the average water temperature along the radius are depicted in Fig. 2(c). We can see that when the element size is smaller than 0.003,

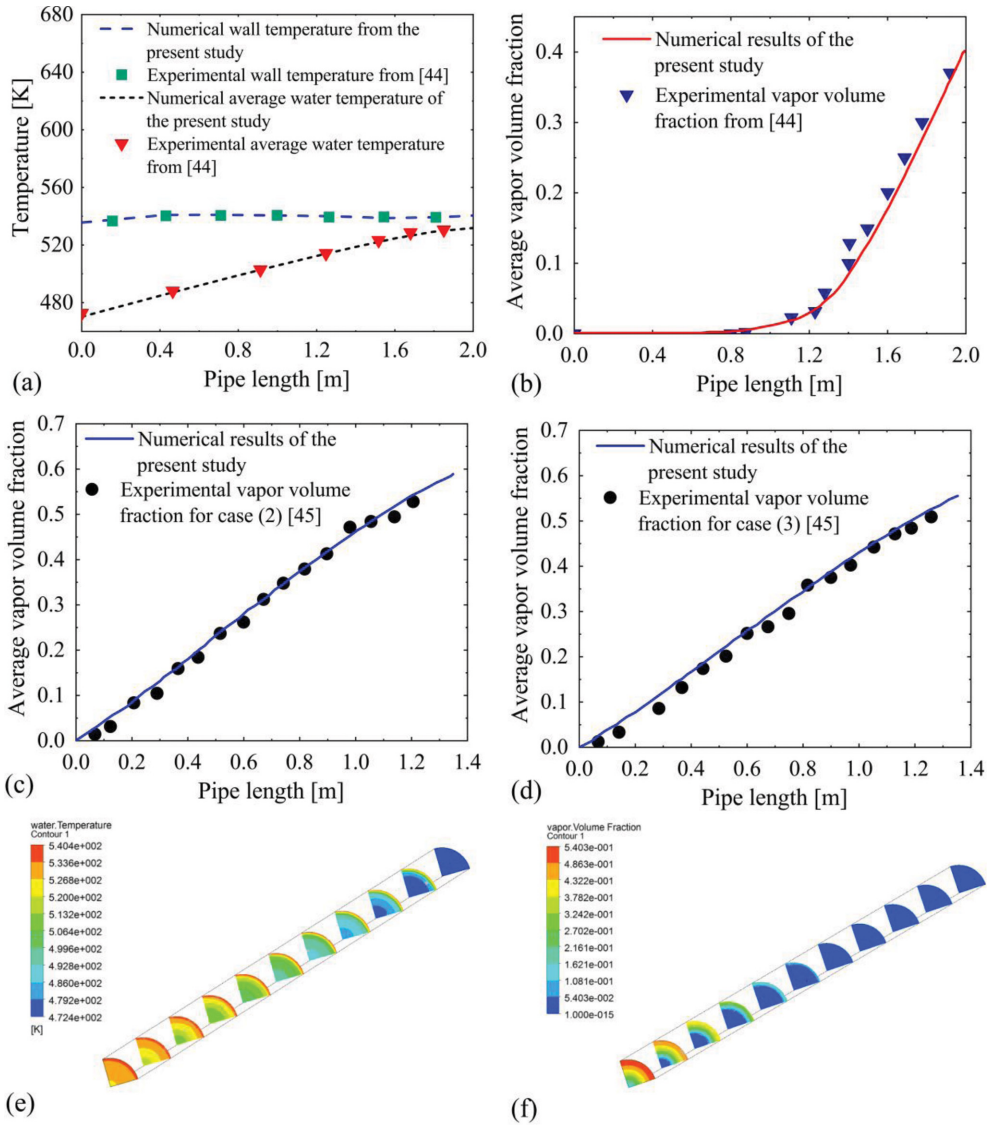



**Fig. 3. Comparison of experimental and numerical values of (a) average water temperature and wall temperature for case (1), vapor volume fraction along the pipe for (b) case (1), (c) case (2), (d) case (3), (e) contour of water temperature, and (f) contour of vapor volume fraction along the pipe.**

the selected quantities remain nearly unchanged, and therefore, the element size of 0.003 is used in the present work.

Fig. 3(a) and Fig. 3(b) show that the numerical results compare well with the experimental results of case (1). Fig. 3(a) depicts the average water temperature and wall temperature. As can be seen, while the average water temperature grows along the pipe, the wall temperature almost remains unchanged. This shows that we are considering the pre-dryout region, otherwise, we would have observed a significant rise in the wall temperature. Moreover, Fig. 3(b) illustrates that the numerical approach in the present study is able to accurately model the onset of boiling in this case. To better validate the numerical simulations two other experimental cases are compared with the present study's results. It is clear that the experimental results of [45] are also in great concordance with the results of the present study. Fig. 3(c) and 3(d) show the comparison of the vapor volume fraction in cases (2) and (3). In addition, the contours of water temperature and vapor volume fraction are presented in Fig. 3(e) and Fig. 3(f) for better visualizing the geometry of the present study. It is clear that through the pipe length the water temperature increases. Also, the vapor generation is clearly marked in Fig. 3(e).

## 5. Objective of Study

A dataset consisting of 408 numerical simulations of subcooled flow boiling was generated with a broad range of boundary conditions to fully capture the characteristics of the flow physics. The parameter coverage is as follows:

- Working fluid: water
- Pressure: 0.7 MPa<P<7 MPa
- Mass flux: 300 kg/m$^2$s< $\dot{m}$ <3,000 kg/m$^2$s
- Heat flux: 0.3 MW/m$^2$<q<2.0 MW/m$^2$
- Subcooled temperature: 10 K<$T_{sub}$<90 K

The objective of this study was to investigate the effects of dif-

ferent boundary conditions on the boiling flow, and subsequently, to build and optimize an artificial neural network to accurately predict the mentioned target quantities. The effects of various "model architectures" are studied to discover the best neural network model for each target quantity. Both average and local parameters are investigated to gain a better understanding of how the flow characteristics differ in each section of the pipe. To properly evaluate the proposed models, a fraction of data points are excluded from the training process and are used to test how well the models are able to predict the quantities of interest.

## ARTIFICIAL NEURAL NETWORK

The artificial neural network is a deep learning method that is designed based on the human neural system. It consists of an input layer, a group of hidden layers, and an output layer through which the feed-forward process occurs. Each layer is comprised of a number of nodes called artificial neurons, which is the basic computational unit in the neural network. As is shown in Fig. 4(a), each neuron receives several signals (called "input"), carry out some calculations on the input signal and their weights, add the bias to the summation of input signals, pass the whole summation to an activation function, and generate one output signal. There are many activation functions such as rectified linear unit (ReLU), Sigmoid, Linear, Softmax, and hyperbolic tangent function. Fig. 4(b) depicts the most common activation functions in regression problems. The most popular choice of activation function seems to be ReLU as it does not suffer from the vanishing gradient problem [46].

To understand how well the model works, the backpropagation technique is used. In this process, after each epoch (i.e., when the feed-forward process completes one pass through the whole training dataset), the loss function is calculated and the weights and biases are updated using a gradient descent optimization to minimize the loss function.

The model selection process is probably the most important section of a neural network because the parameters investigated and the decisions made in this section directly affect the final output of the model. To discover the ideal model, we should investigate and optimize different architectures and hyperparameters, including the number of input parameters, number of neurons, number of hidden layers, activation functions, and loss functions [47]. Note that the deepest and the largest network possible would not necessarily be the best choice. For example, a neural network with a few numbers of hidden layers cannot perform sufficiently well. On the other hand, by excessively increasing the hidden layers, the model would fall into the over-fitting problem.

Fig. 5 presents the model used in the present study. Prior to constructing the ANN, the data are preprocessed. The input parameters are normalized in a range of zero to one. The dataset is split into training and test data with a 70%-30% split ratio. For the average parameters, there are 242 training data points and 104 test data points. To generate the datasets for the local parameters, the target quantities are extracted in 11 different cross sections throughout the pipe. After the data preprocessing and cleansing, we have 800 training data points and 344 test points for the heat transfer parameters, and 2289 training data points and 982 test data points for the bubble dynamics parameters.

Table 2 shows the optimized ANN's hyperparameters used in the present study. The learning rate is set to 0.001. Of course, larger values could be chosen to achieve convergence faster, but this could, simultaneously, cause disturbance near the optimum point. The Adam optimizer [48] was selected as the gradient descent solver in this study. Finally, the exponential first and second moment vector was set to be 0.9 and 0.999, respectively.

We used the mean squared error (MSE) as the loss function, which is calculated as:

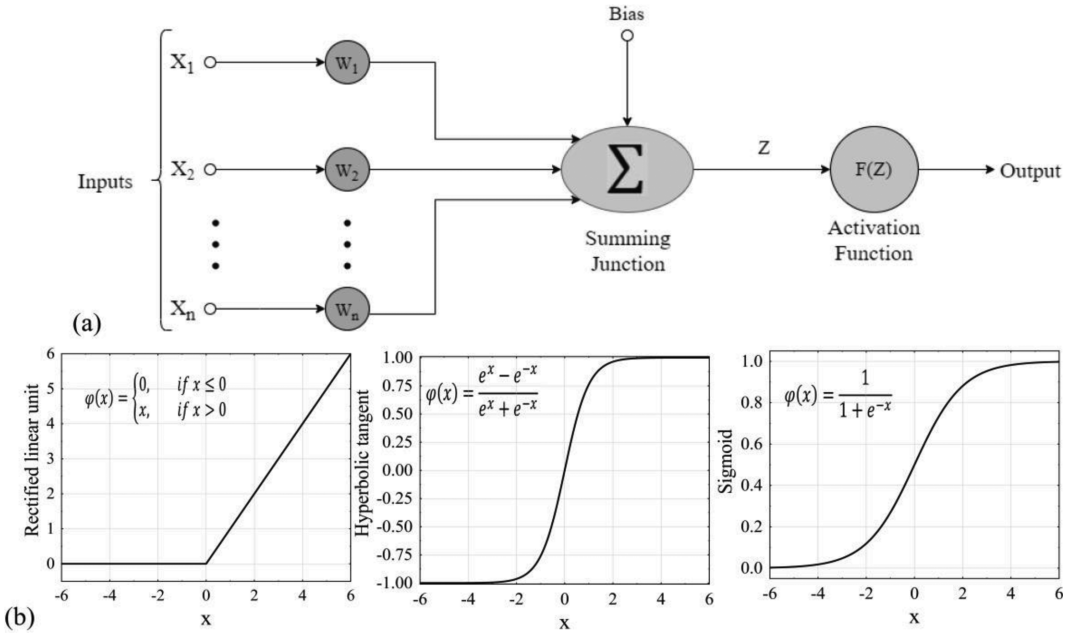



**Fig. 4. (a) A schematic model of an artificial neuron and (b) The most common activation functions for regression problem.**

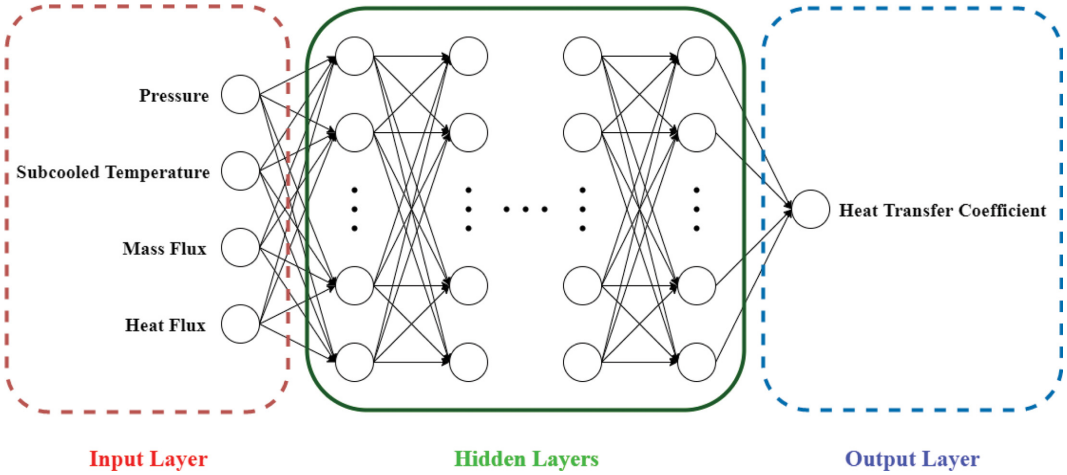



**Fig. 5. The ANN model utilized in the present study.**

**Table 2. ANN model parameters chosen in the present study**

| Parameters | Values |
|---|---|
| Activation functions | ReLU, Sigmoid, Linear |
| Optimizer | Adam |
| Batch size | Varies in every case |
| Learning rate | 0.001 |
| Exponential decay rate of first moment vector | 0.9 |
| Exponential decay rate of second moment vector | 0.999 |
| Loss function | Mean squared error |

**Table 3. The case studies investigated in the present study**

| Case study | Pressure [MPa] | Heat flux [MW/m$^2$K] | Mass flux [kg/m$^2$s] | Subcooled temperature [K] |
|---|---|---|---|---|
| 1 | 0.7-7.0 | 0.57 | 900 | 58.2 |
| 2 | 7.0 | 0.3-1.5 | 900 | 30 |
| 3 | 4.5 | 1.0 | 600-1,500 | 40 |
| 4 | 0.7 | 0.3 | 600 | 30-58.2 |

$$E_m = \frac{1}{n}\sum_{i=1}^{n}(Y_i - \hat{Y}_i)^2 \quad (21)$$

The model accuracy is based on the mean absolute error (MAE), which is measured as:

$$MAE = \frac{1}{n}\sum_{t=1}^{n}\frac{|Y_i - \hat{Y}_i|}{Y_i} \times 100\% \quad (22)$$

In Eqs. (21) and (22), n is the number of data points, $Y_i$ is the real value of the target quantity, and $\hat{Y}_i$ is the predicted value of the target quantity by the ANN.

We use the coefficient of determination (R-squared or $R^2$) to show how well the model is capable of predicting the target quantity. If $\overline{Y}$ is the mean of the data, $R^2$ is defined as:

$$R^2 = 1 - \frac{\Sigma(Y_i - \hat{Y}_i)^2}{\Sigma(Y_i - \overline{Y})} \quad (23)$$

The $R^2$ value ranges between 0 and 1, where zero is the case when the model is unable to predict the target quantities. On the contrary, the R-squared of one is equivalent to the best model, which predicts all the cases correctly.

## RESULTS AND DISCUSSION

We present two categories of the results: those from the numerical simulations and those from the ANN models. In addition, to confirm the data are valid, a verification of the extracted data is presented based on the experimental results.

### 1. Numerical Simulations

The effects of different boundary conditions on thermal characteristics and bubble dynamics of subcooled flow boiling were investigated. To make the comparison simpler, certain case studies were selected and used throughout this work. Table 3 presents the mentioned case studies.

1-1. Wall Temperature

Fig. 6 depicts the changes of wall temperature with respect to pressure, heat flux, mass flux, and inlet subcooled temperature variations along the pipe in different case studies.

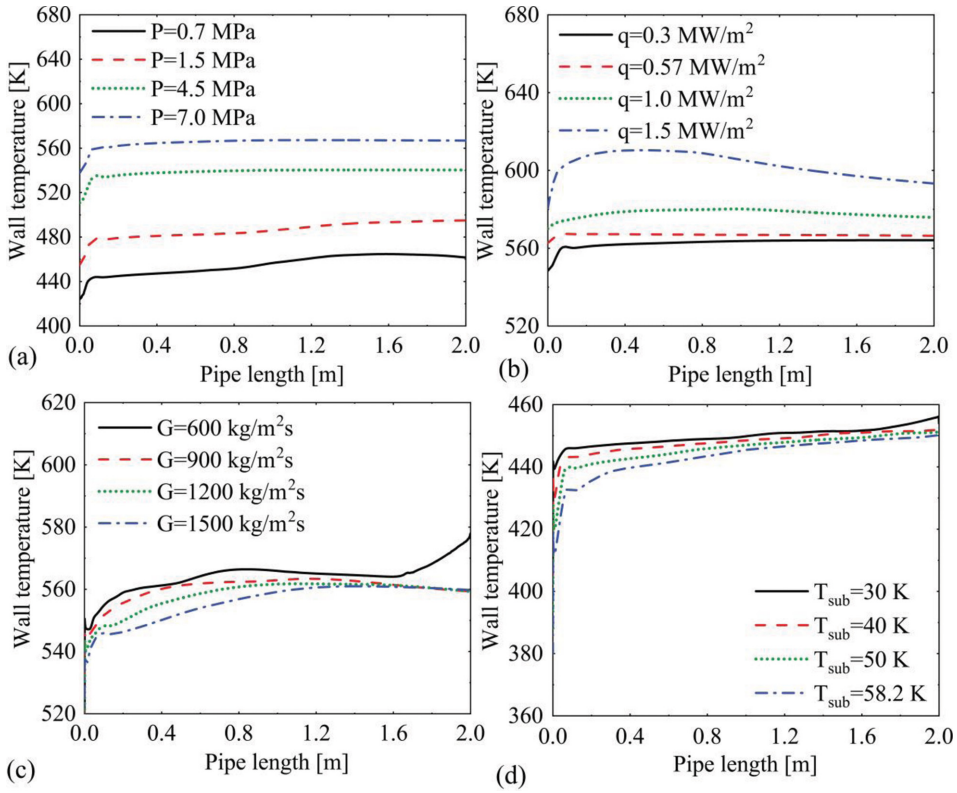



**Fig. 6. Comparison of wall temperature in (a) case study 1 with different pressures, (b) case study 2 with different heat fluxes, (c) case study 3 with different mass fluxes, and (d) case study 4 with different subcooled temperatures.**

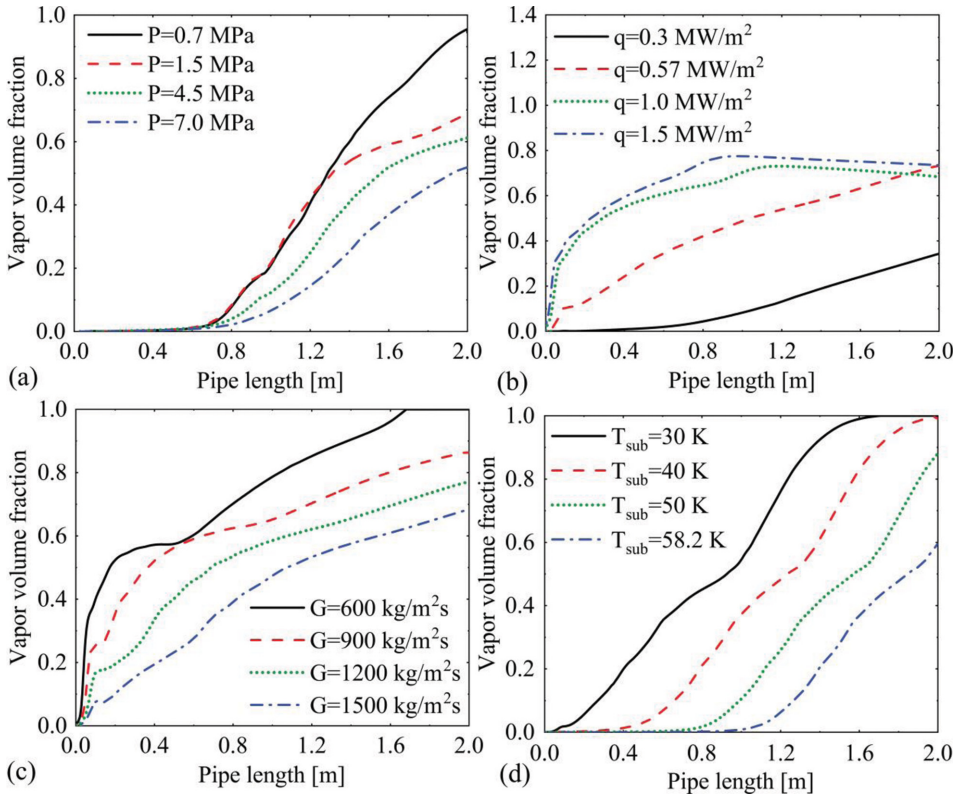



**Fig. 7. Comparison of vapor volume fraction in (a) case study 1 with different pressures, (b) case study 2 with different heat fluxes, (c) case study 3 with different mass fluxes, and (d) case study 4 with different subcooled temperatures.**

Fig. 6(a) shows the variation of case study 1 by changing the pressure of the working fluid. As pressure increases, the wall temperature also increases due to the rise in the fluid saturation temperature [49]. Besides, the onset of boiling occurs if the wall temperature is higher than the fluid saturation temperature [50]. The same pattern is illustrated in Fig. 6(b) for case study 2. It is observed that by applying a higher heat flux to the wall, the wall reaches a higher temperature. Fig. 6(c) depicts the effects of mass flux for case study 3. It is evident that as the mass flux rises, the wall temperature drops. When the mass flux is 600 kg/m$^2$s, there is a sudden augmentation towards the end of the pipe. This problem could be addressed by pointing out that towards the end of the pipe, as is shown in Fig. 7(c), the vapor volume fraction is equal to 1. Since the heat transfer coefficient is dropped significantly owing to the loss of two-phase-flow heat transfer mechanism, we observe a significant increase in wall temperature. Fig. 6(d) demonstrates the influence of inlet liquid subcooled temperature variation in case study 4. The wall temperature decreases by increasing the inlet subcooled temperature although the variation seems to be minor when compared to the other contributing factors. Basu et al. [51] also observed this variation with more focus on the nucleation site density, and their results verify the trend in Fig. 6(d).

1-2. Vapor Volume Fraction

Fig. 7 shows the effects of different parameters on vapor volume fraction. As can be seen in Fig. 7(a), pressure increase inversely affects the vapor generation process. The reason for this is that by increasing the pressure, the saturation temperature rises as well. Consequently, the majority of the heat flux is devoted to increasing the fluid temperature rather than causing the onset of boiling. Fig. 7(b) indicates the effect of heat flux on the vapor volume fraction along the pipe. It is evident that as the heat flux applied to the pipe wall rises, the vapor volume fraction increases significantly. However, in two cases, the increasing trend stops and levels off. This usually happens when the flow pattern changes to slug flow in which case the vapor generation rate decreases [52]. Fig. 7(c) and Fig. 7(d) show that the increase in the mass flux and the inlet subcooled temperature inversely affects the vapor generation. Note that in Fig. 7(d), as the inlet subcooled temperature increases, the onset of boiling is delayed.

1-3. Bubble Departure Diameter

Fig. 8 shows how bubble departure diameter varies along the pipe as the contributing parameters change. The bubble departure diameter is of great importance since it plays a significant role in heat flux partitioning [53]. Fig. 8(a) shows that the bubble departure diameter decreases as the pressure increases. The basis of most of the models for bubble departure size is the Fritz model in pool boiling [54]. All other models are mainly incorporating other forces to take more complexities into account. Bubble departure diameter is highly dependent on wall superheat [55], so by increasing the pressure level in the working fluid, the saturation temperature increases, thereby resulting in lower wall superheats. Therefore, the bubble departure diameter decreases as the pressure augments. Fig. 8(b) depicts the heat flux dependency of bubble departure diameter, showing the opposite effect when compared to the pressure variation. Since bubble departure is highly dependent on wall superheat, by increasing the heat flux, the wall superheat increases, thus,

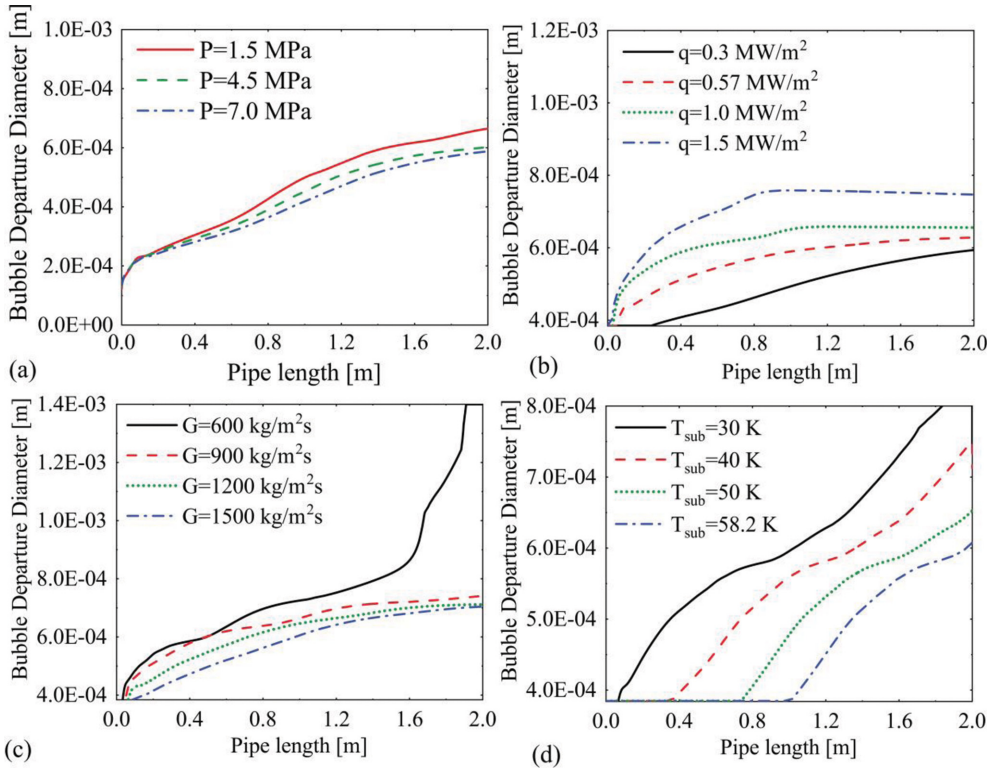



**Fig. 8. Comparison of bubble departure diameter in (a) case study 1 with different pressures, (b) case study 2 with different heat fluxes, (c) case study 3 with different mass fluxes, and (d) case study 4 with different subcooled temperatures.**

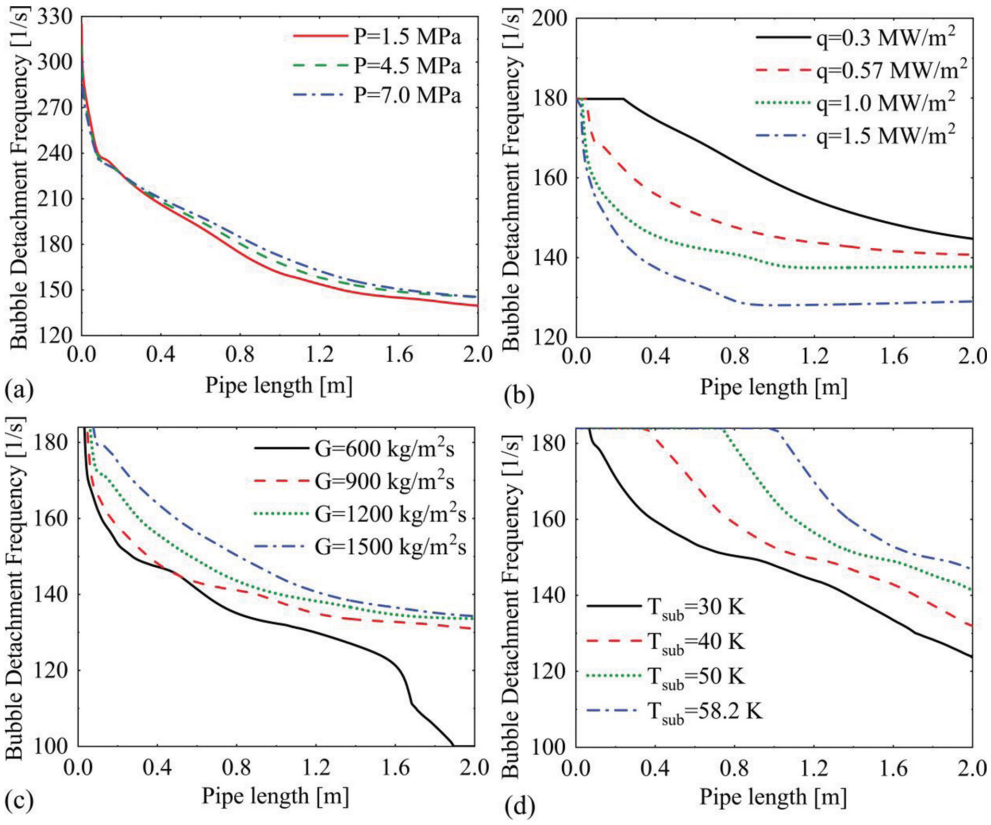



**Fig. 9. Comparison of bubble detachment frequency in (a) case study 1 with different pressures, (b) case study 2 with different heat fluxes, (c) case study 3 with different mass fluxes, and (d) case study 4 with different subcooled temperatures.**

resulting in bigger bubble departure diameters. Similar to vapor volume fraction, the bubble departure diameter drops as the mass flux, and the inlet subcooled temperature augment, as shown in Fig. 8(c) and Fig. 8(d), respectively. The same trend is observed in [56,57].

1-4. Bubble Detachment Frequency

Fig. 9 presents the numerical results of bubble detachment frequency. According to Equation 15, bubble detachment frequency is inversely related to bubble departure diameter. Therefore, it is logical to observe the inverse pattern in Fig. 9 compared to Fig. 8. In addition, according to [55], bubble departure frequency is highly dependent on wall superheat; therefore, we would observe more variations in cases where wall superheat is altered. Fig. 9(a), Fig. 9(c), and Fig. 9(d) show that the bubble detachment frequency increases due to the augmentation in pressure, mass flux, and inlet subcooled temperature, respectively. The heat flux rise, however, presents the opposite pattern, showing a drop in the bubble detachment frequency, as shown in Fig. 9(b). The most significant impact is caused by changing the heat flux as it significantly affects wall superheat. The results observed for bubble detachment frequency agree well with the experimental study of Yoo et al. [57].

1-5. Bubble Detachment Waiting Time

Bubble detachment waiting time is the heating time needed for the thermal boundary layer thickness to re-grow to 3/2 times the cavity sizes [58]. However, in boiling, waiting time is defined as the time from the departure of one bubble until the appearance of another bubble in one nucleation site.

Since the bubble detachment waiting time is inversely proportional to bubble detachment frequency, formulated in Equation 16, an opposite pattern for the bubble detachment waiting time is observed when it is compared to the bubble detachment frequency. Fig. 10 illustrates the variation of the bubble detachment waiting time in different cases along the pipe length. As can be seen from Fig. 10(a), as the fluid pressure increases, the bubble detachment waiting time decreases. Inversely, this parameter increases with an augmentation in the heat flux, presented in Fig. 10(b). Clearly, the largest variation is caused by changing heat flux as a result of its significant effect on wall superheat. Moreover, Fig. 10(c) and Fig. 10(d) depict the decreasing trend of the bubble detachment waiting time by increasing the mass flux and the inlet subcooled temperature, respectively. The irregular pattern in Fig. 10(c) is due to dryout. As the volume fraction has reached its maximum value, as shown in Fig. 7(c), the waiting time has significantly increased.

1-6. Nucleation Site Density

The nucleation site density is one of the significant parameters in bubble dynamics of boiling processes. It is highly dependent on the wall heat flux, wall superheat, and the number of cavities. Fig. 11 presents the nucleation site density in logarithmic scale. Fig. 11(a) depicts the variations of this parameter when the working fluid pressure is changed. The nucleation sites substantially drop when the pressure is increased. The main reason for this trend is that as the fluid pressure increases, the number of active cavities

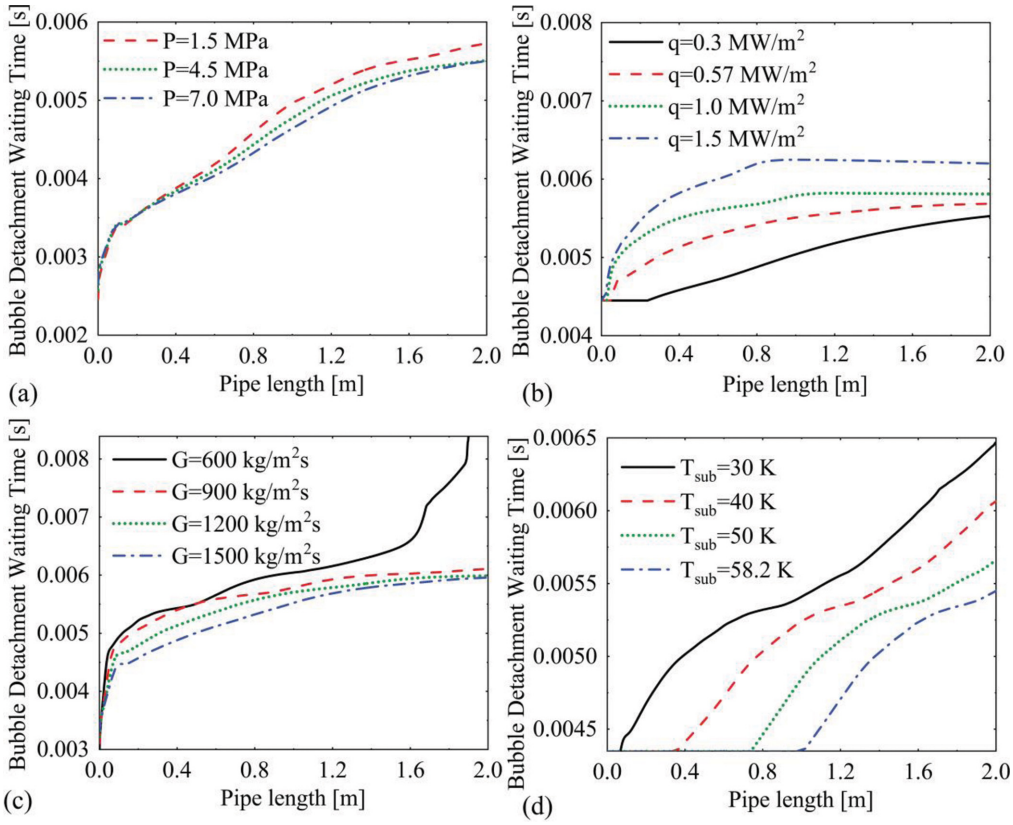



**Fig. 10. Comparison of bubble detachment waiting time in (a) case study 1 with different pressures, (b) case study 2 with different heat fluxes, (c) case study 3 with different mass fluxes, and (d) case study 4 with different subcooled temperatures.**

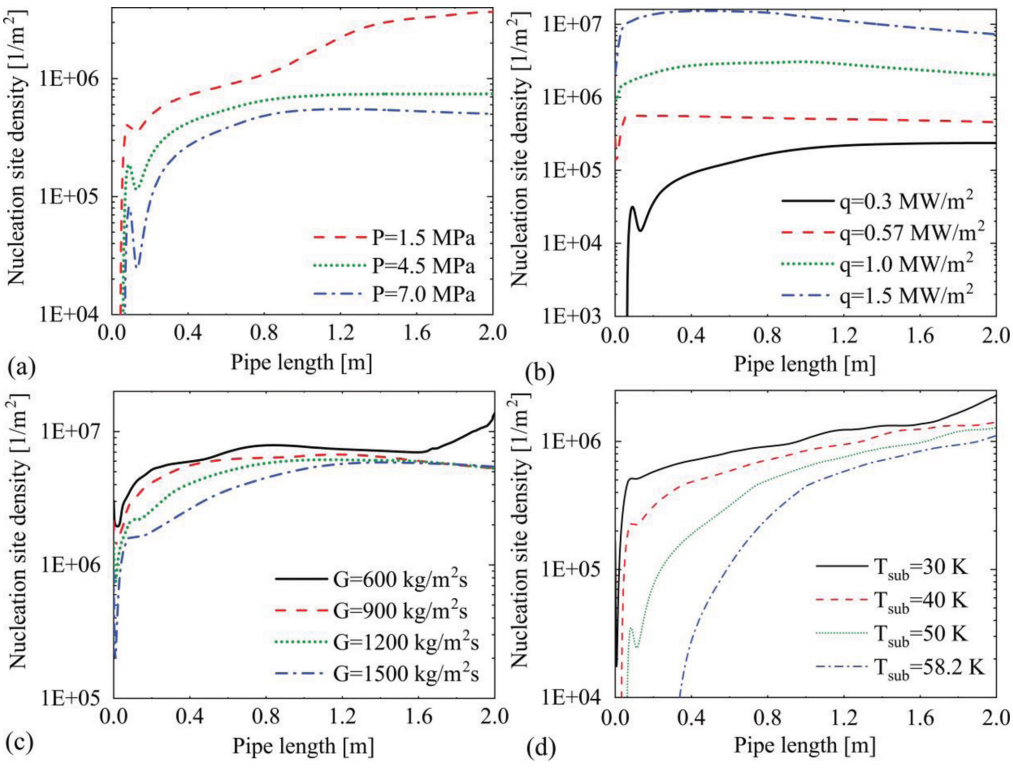



**Fig. 11. Comparison of nucleation site density in (a) case study 1 with different pressures, (b) case study 2 with different heat fluxes, (c) case study 3 with different mass fluxes, and (d) case study 4 with different subcooled temperatures.**

**Table 4. ANN model predictions for fixed input parameters and different combinations of hidden layers**

| Test case | Input parameters | ANN model hidden layers | MAE (%) | $R^2$ |
|---|---|---|---|---|
| 1 | P, q, ṁ, $T_{sub}$, $X_{in}$ | (32) | 0.28% | 1 |
| 2 | | (32,64) | 0.14% | 1 |
| 3 | | (32,64,32) | 0.14% | 1 |
| 4 | | (32,64,64,32) | 0.14% | 1 |
| 5 | | (32,64,128,64,32) | 0.20% | 1 |
| 6 | | (32,64,128,128,64,32) | 0.14% | 1 |
| **7*** | | **(32,64,128,256,128,64,32)** | **0.11%** | **1** |
| 8 | | (32,64,128,256,256,128,64,32) | 0.36% | 1 |
| 9 | | (32,64,128,256,512,256,128,64,32) | 0.13% | 1 |

*Finally selected model.

**Table 5. ANN model predictions for fixed ANN model and different activation functions for the output layer**

| Test case | ANN model | Output activation function | MAE (%) | $R^2$ |
|---|---|---|---|---|
| 1 | (32,64,128,256,128,64,32) | Linear | 0.12% | 1 |
| **2*** | | **ReLU** | **0.11%** | **1** |
| 3 | | Sigmoid | 0.14% | 1 |

*Finally selected model.

decreases [59]. Fig. 11(b) shows that the augmentation of the applied heat flux significantly increases the number of active nucleation sites. The reason for a gradual drop in the number of nucleation sites towards the end of the pipe is mainly the coalescence of the bubbles, which forms a layer of vapor adjacent to the wall, thus deactivating nucleation sites. However, as shown in Fig. 11(c) and Fig. 11(d), the number of nucleation sites decreases as the mass flux and the inlet subcooled temperature increase. This is because by increasing the inlet subcooled temperature, more heat flux is required to increase the bulk temperature, and it inversely affects the boiling process. The significant increase in Fig. 11(c) for the mass flux of 600 $Kg/M^2s$ could be justified by the trend of the same mass flux in Fig. 7(c). Since the vapor volume fraction reaches its maximum value, meaning there is only vapor in the flow, the number of nucleation sites would dramatically decrease. The presented trends for nucleation site density in the present study are verified with the results of Yoo et al. [57].

**2. ANN Results**

An artificial neural network was utilized to predict ten different parameters. As mentioned earlier, the process of choosing the best model that could predict a target quantity is a procedure that must be carried out carefully. Thus, we carried out a hyperparameters tuning procedure for each of the target quantities. In the next section, as an example, the procedure associated with local wall temperature is presented. The same procedure was followed for every target quantity in this study.

2-1. The ANN Model Selection Procedure

After the preprocessing stage, the local wall temperature dataset consists of 1144 numerical results. The results coverage is the same as in Table 1. The dataset is split into training and test data points with a 70%-30% split ratio, resulting in 800 training data points and 344 test data points. The next step is to determine the number of the hidden layers. The widely used doubling sequence is utilized for the number of hidden layers, starting with 32 neurons. To begin with the process, the number of neurons and the number of hidden layers must be investigated as they are the principal components of the neural network. Table 4 presents the results for different numbers of neurons and hidden layers, using ReLU as the activation function of all layers.

It is obvious that by increasing the number of neurons and the number of hidden layers, the model becomes more accurate; however, this improvement is stopped, and an opposite pattern is observed when overfitting occurred. Therefore, the selected model is (32,64,128,256,128,64,32). After selecting the number of hidden layers, the impact of different activation functions for the output layer is investigated in Table 5.

Apparently, using both Linear and ReLU results in the same MAE. However, for the sake of consistency, the ReLU activation function is utilized for the local wall temperature.

Another contributing element in the model architecture is the batch size, i.e., the number of data points going through the feed-forward process before the backpropagation begins. Thus, the batch size is the number of data points that are processed in the neural network before the weights and biases are updated. According to Table 6, the mean absolute error of both batch sizes of 8 and 16 is the same. However, the selected batch size is 16 because this choice is less time-consuming.

Finally, the number of epochs are compared with each other, as shown in Table 7. The best choice is the model with 20,000 epochs. The reason that 20,000 is picked over 30,000 or higher epochs despite the same MAEs is that the computational expenses in the former are way less than the later ones.

It is evident that the best choice for hyperparameters is not necessarily the deepest ANN or the slowest model, so it is logical that a search for the best model architecture should be done prior to model selection. This selection procedure is carried out to identify

**Table 6. ANN model predictions for a fixed number of hidden layers and different batch size**

| Test case | ANN model | Batch size | MAE (%) | $R^2$ |
|---|---|---|---|---|
| 1 | (32,64,128,256,128,64,32) | 2 | 0.22% | 1 |
| 2 | | 4 | 0.17% | 1 |
| 3 | | 8 | 0.11% | 1 |
| **4*** | | **16** | **0.11%** | **1** |
| 5 | | 32 | 0.17% | 1 |
| 6 | | 64 | 0.17% | 1 |

*Finally selected model.

**Table 7. ANN model predictions for a fixed number of hidden layers and different numbers of epochs**

| Test case | ANN model | Number of epochs | MAE (%) | $R^2$ |
|---|---|---|---|---|
| 1 | (32,64,128,256,128,64,32) | 1,000 | 0.11% | 1 |
| 2 | | 2,000 | 0.10% | 1 |
| 3 | | 5,000 | 0.08% | 1 |
| 4 | | 10,000 | 0.13% | 1 |
| **5*** | | **20,000** | **0.07%** | **1** |
| 6 | | 30,000 | 0.07% | 1 |
| 7 | | 40,000 | 0.07% | 1 |
| 8 | | 50,000 | 0.07% | 1 |

*Finally selected model.

**Table 8. Finally selected models**

| Output parameter | Input parameters | ANN model | Number of epochs | Batch size | Activation function |
|---|---|---|---|---|---|
| Average wall temperature | P, q, $\dot{m}$, $T_{sub}$ | (128,64,32) | 40,000 | 32 | ReLU |
| Average vapor volume fraction | P, q, $\dot{m}$, $T_{sub}$ | (256,128,64,32) | 30,000 | 8 | ReLU |
| Average heat transfer coefficient | P, q, $\dot{m}$, $T_{sub}$ | (256,128,64,32) | 30,000 | 16 | ReLU |
| Local wall temperature | P, q, $\dot{m}$, $T_{sub}$, $X_{in}$ | (32,64,128,256,128,64,32) | 20,000 | 16 | ReLU |
| Local vapor volume fraction | P, q, $\dot{m}$, $T_{sub}$, $X_{in}$ | (128,64,32) | 10,000 | 8 | Linear |
| Local heat transfer coefficient | P, q, $\dot{m}$, $T_{sub}$, $X_{in}$ | (32,64,32) | 20,000 | 16 | ReLU |
| Bubble departure diameter | P, q, $\dot{m}$, $T_{sub}$, $X_{in}$ | (32,64,128,64,32) | 10,000 | 32 | ReLU |
| Bubble detachment frequency | P, q, $\dot{m}$, $T_{sub}$, $X_{in}$ | (128,128,64,64,32,32) | 10,000 | 64 | Linear |
| Bubble detachment waiting time | P, q, $\dot{m}$, $T_{sub}$, $X_{in}$ | (256,128,64,32) | 8,000 | 64 | ReLU |
| Nucleation site density | P, q, $\dot{m}$, $T_{sub}$, $X_{in}$ | (128,128,64,64,32,32) | 40,000 | 32 | ReLU |

the best model architecture for every single target quantity in this study. The final selected models for all of the quantities of interest are presented in Table 8. These models achieve the best performance among the examined cases.

2-2. The ANN Model's Performance Evaluation

As mentioned in Table 8, the inputs for average and local parameters are P, q, $\dot{m}$, $T_{sub}$ and P, q, $\dot{m}$, $T_{sub}$, $X_{in}$, respectively. The logic behind selecting these input parameters is that they fully cover the components causing the boiling process. For instance, pressure is a good representative of fluid properties. The heat flux, mass flux, and subcooled temperature directly affect the subcooled flow boiling. Additionally, it is essential to use the entrance length as the input parameter for local target quantities. We investigated the ANN performance in four different categories: heat transfer coefficient, vapor volume fraction, wall temperature, and bubble dynamics. The test dataset is used to evaluate the accuracy of the ANN models in the following. To better demonstrate the deviation of each proposed models from the ideal case, a linear regression is fitted to the predicted results. The ideal case is where all the data points are located along the y=x line.

2-2-1. Heat Transfer Coefficient

For the average heat transfer coefficient, 348 data points were utilized. This dataset is divided into 243 data points for training and 105 data points for testing the model. Fig. 12(a) shows the predicted heat transfer coefficient against the numerical results for the 105 test data points. The proposed ANN model is able to achieve an MAE of 1.27%, and the $R^2$ was as high as 0.97.

The local heat transfer coefficient dataset consists of 1144 data points. This dataset is split into 800 data points for training and 344 data points for testing. Fig. 12(b) indicates the model predic-

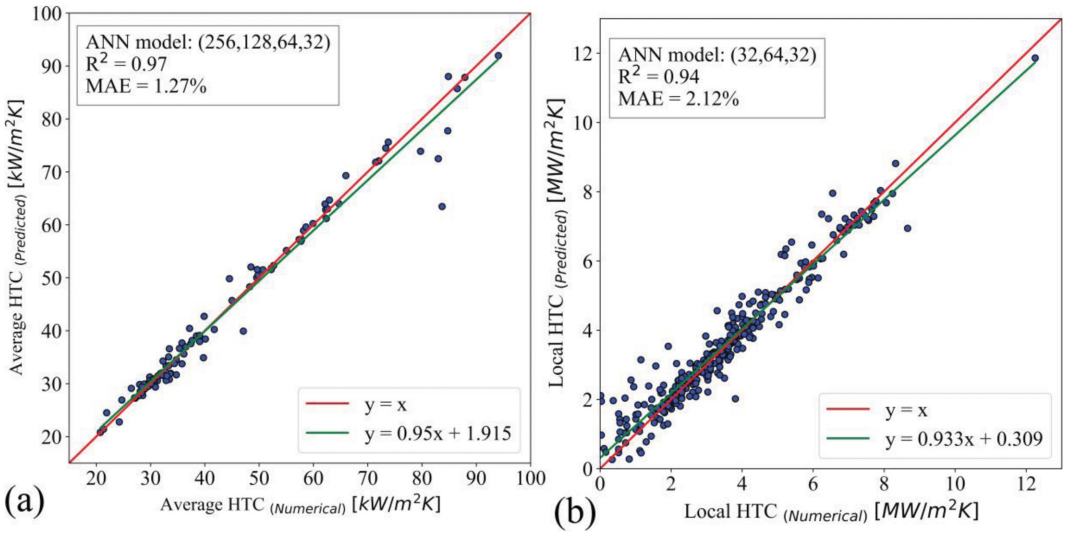



**Fig. 12. ANN model prediction of (a) 105 data points of average heat transfer coefficient for the hidden layer formation of (256,128,64,32) and input parameters of P, q, $\dot{m}$, $T_{sub}$, and (b) 344 data points of local heat transfer coefficient for hidden layer formation of (32,64,32) and input parameters of P, q, $\dot{m}$, $T_{sub}$, $X_{in}$.**

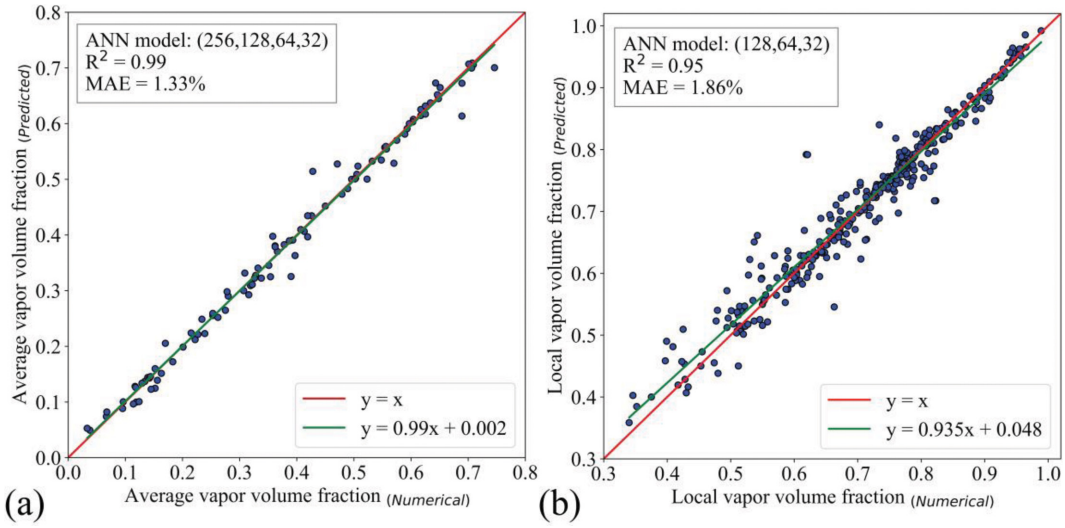



**Fig. 13. ANN model prediction of (a) 105 data points of average vapor volume fraction for the hidden layer formation of (256,128,64,32) and input parameters of P, q, $\dot{m}$, $T_{sub}$ and (b) 344 data points of local vapor volume fraction for hidden layer formation of (128,64,32) and input parameters of P, q, $\dot{m}$, $T_{sub}$, $X_{in}$.**

tion of the local heat transfer coefficient for the 344 test data points. The extracted results reveal that this model is able to get the MAE of 2.12% and the $R^2$ of 0.94. It is clear that the deviations from the ideal case are quite more than the average case, and that is why the MAE is larger in the local case.

In both cases, the green lines (i.e. linear regression lines) are reasonably similar to the ideal case, which shows how accurate the models are.

2-2-2. Vapor Volume Fraction

The ANN model predictions for the average and local vapor volume fraction are presented in Fig. 13(a) and (b), respectively. In the case of the average vapor volume fraction in Fig. 13(a), the model seems to perform well since the MAE is 1.33%, and the $R^2$ equals 0.99. Fig. 13(b) illustrates the ANN result for local vapor volume fraction with the MAE of 1.86% and $R^2$ as high as 0.95.

The model for average vapor volume fraction is so accurate that the linear regression of the results perfectly fits the ideal case. For local vapor volume fraction, however, there is a slight deviation from the ideal case. In both cases, the mathematical equations of linear regressions are available.

2-2-3. Wall Temperature

The wall temperature is one of the most crucial parameters of flow boiling processes because an uncontrollable increase in this parameter could lead to a burnout and, as a result, the fluid would get out of the pipe, resulting in catastrophic consequences if the fluid was poisonous. Therefore, a model that is capable of accurately

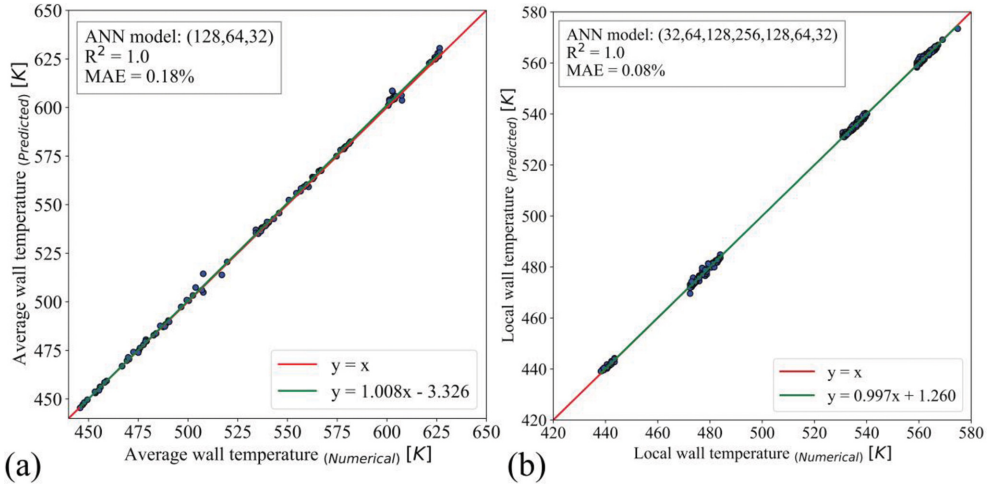



**Fig. 14. ANN model prediction of (a) 105 data points of average wall temperature for the hidden layer formation of (256,128,64,32) and input parameters of P, q, ṁ, $T_{sub}$ and (b) 344 data points of local wall temperature for hidden layer formation of (32,64,128,256,128,64,32) and input parameters of P, q, ṁ, $T_{sub}$, $X_{in}$.**

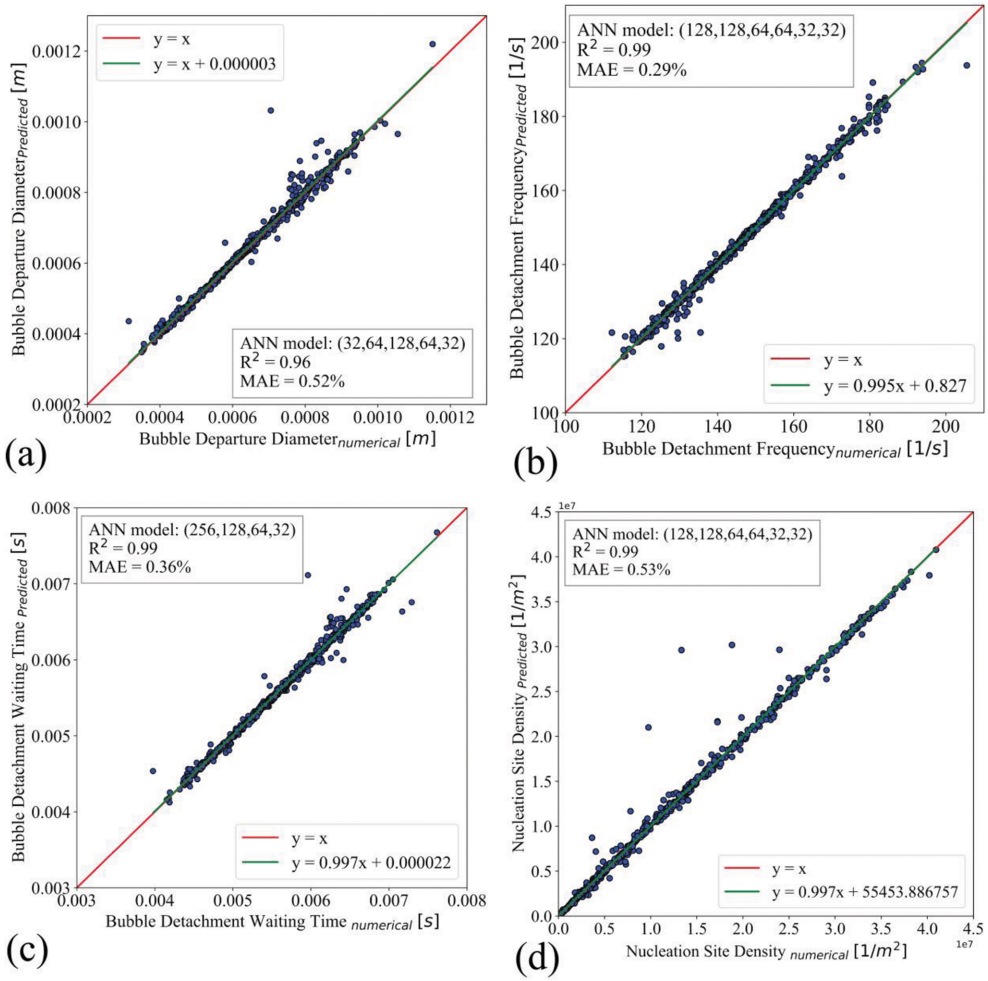



**Fig. 15. ANN model prediction of 982 data points of (a) local bubble departure diameter for the hidden layer formation of (32,64,128,64,32) and input parameters of P, q, ṁ, $T_{sub}$, $X_{in}$, (b) local bubble detachment frequency for hidden layer formation of (128,128,64,64,32,32) and input parameters of P, q, ṁ, $T_{sub}$, $X_{in}$, (c) local bubble detachment waiting time for hidden layer formation of (256,128,64,32) and input parameters of P, q, ṁ, $T_{sub}$, $X_{in}$, and (d) nucleation site density for hidden layer formation of (128,128,64,64,32,32) and input parameters of P, q, ṁ, $T_{sub}$, $X_{in}$.**

predicting this parameter is of great benefit. Fig. 14(a) indicates the results of the model for average wall temperature. This model shows the MAE of 0.18% and the $R^2$ of 1.0. Fig. 14(b) shows the comparison of the predicted and numerical local wall temperature. Since the wall temperature is highly dependent on the pressure of the working fluid, the four clusters of data points represent four different pressures. The model for this target quantity was able to achieve the MAE as low as 0.08% and maintain the $R^2$ to 1.0. Additionally, the linear regressions of the results depict a great agreement with the ideal case.

2-2-4. Bubble Dynamics Parameters

To fully understand the bubble dynamics of the boiling process, we investigated relevant parameters, such as bubble departure diameter, bubble detachment frequency, bubble detachment waiting time, and nucleation site density. The dataset used in this section is comprised of 3271 data points. This dataset is split with a ratio of 70%-30%, resulting in 2289 training data points and 982 testing data points.

Fig. 15(a) illustrates the ANN model predictions of bubble departure diameter with P, q, $\dot{m}$, $T_{sub}$, $X_{in}$ as inputs. The model achieves the MAE of 0.52% and the $R^2$ of 0.96. In Fig. 15(b), the bubble detachment frequency model is presented. The input parameters include P, q, $\dot{m}$, $T_{sub}$, $X_{in}$. The MAE and $R^2$ of this model are 0.29% and 0.99, respectively. The MAE for this parameter is the lowest among the bubble dynamics parameters and, hence, this model has the most accurate predictions among the mentioned target quantities. Fig. 15(c) and Fig. 15(d) illustrate the models for bubble detachment waiting time and nucleation site density, respectively. The MAE and $R^2$ for bubble detachment waiting time are 0.36% and 0.99, respectively. Similarly, the mentioned metrics for nucleation site density are 0.53% and 0.99, respectively. To show how accurate the models perform, we used a fitted linear regression for each quantity. The linear regressions perfectly resemble the ideal case, showing the high accuracy of the proposed models.

2-2-5. The ANN Model's Predictions

To fully understand how well the ANN models are able to predict the target quantities, a number of test data points were used to evaluate the models' performance. Fig. 16 and Fig. 17 compare the numerical results with the predicted ones for the heat transfer and bubble dynamics quantities. As can be seen, the ANN models are

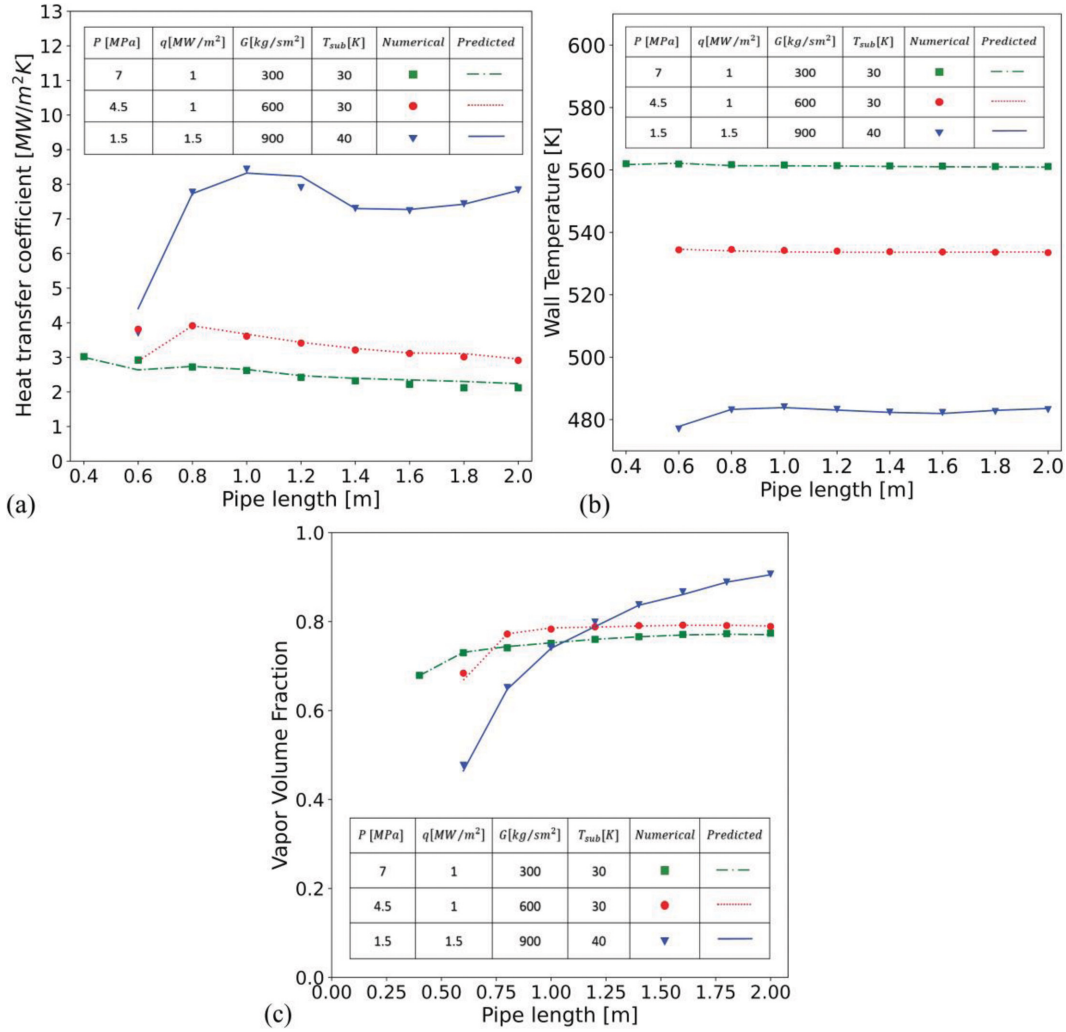



**Fig. 16. ANN model's prediction of the excluded data points for (a) local heat transfer coefficient, (b) local wall temperature, and (c) local vapor volume fraction.**

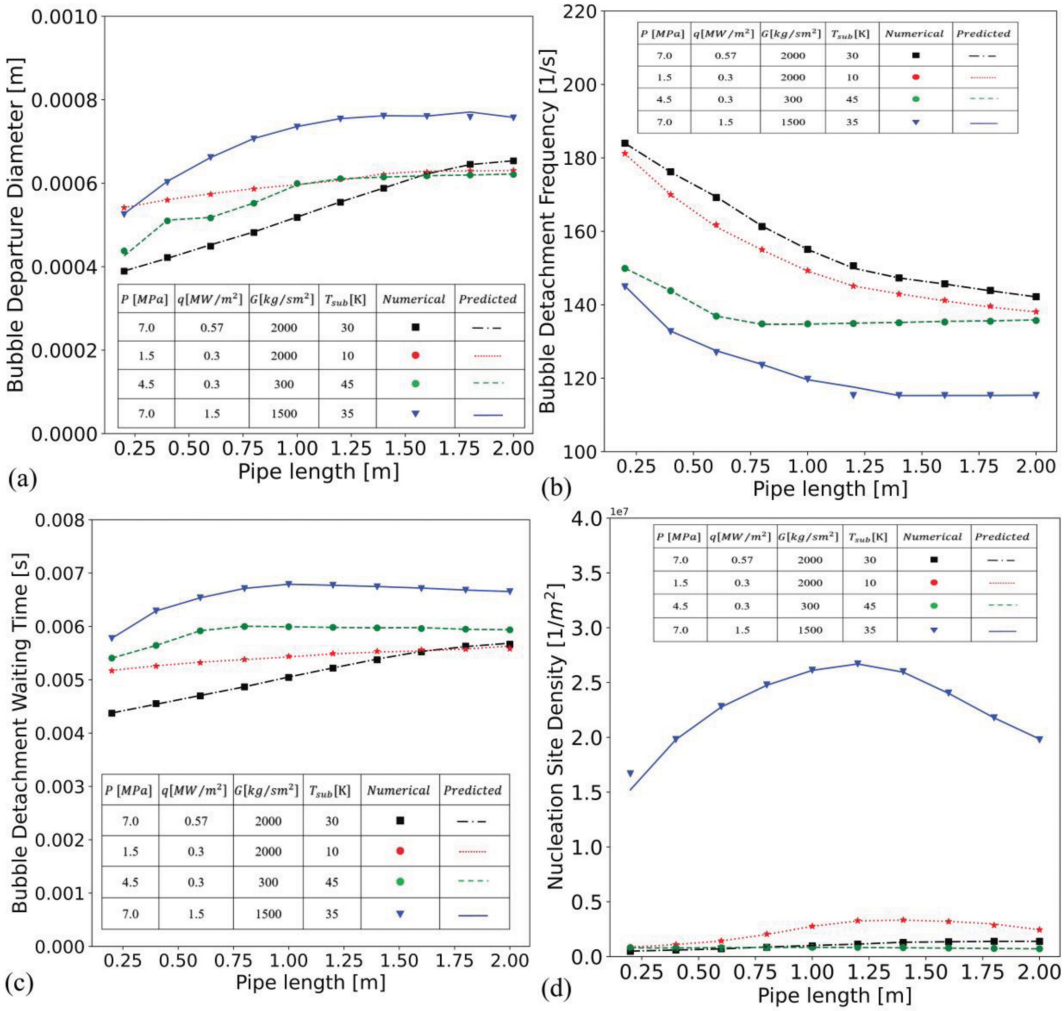



**Fig. 17. ANN models prediction of the excluded data points for (a) bubble departure diameter, (b) bubble detachment frequency, (c) bubble detachment waiting time, and (d) nucleation site density.**

able to correctly capture the variations of different target quantities along the pipe. The data used in Fig. 16 is distributed all over the solution domain to ensure that the models have the ability to give accurate predictions in various flow conditions.

Fig. 17 shows the ANN model prediction of bubble dynamics. It is evident that for almost all the cases the ANN model is capable of predicting the target quantities similar to the real value.

## CONCLUSION

The three-dimensional numerical simulation of subcooled flow boiling of water based on the Euler-Euler approach was performed. A wide range of values of boundary conditions including the pressure, heat flux, mass flux, and inlet liquid subcooled temperature was used to generate 408 cases. The variation of boundary conditions caused different patterns in the quantities of interest. Wall temperature increased by increasing the pressure and the heat flux. However, it was reduced by increasing the mass flux and the inlet subcooled temperature. The vapor volume fraction increased by the augmentation of heat flux, while the rise in pressure, mass flux, and inlet subcooled temperature caused a significant drop in this quantity. Also, the bubble dynamics parameters such as bubble departure diameter, bubble detachment frequency, bubble detachment waiting time, and nucleation site density experienced some variations due to changing the boundary conditions. The data extracted from the numerical results were split into training and test datasets. The ANN hyperparameters were carefully tuned to select the best model for each target quantity. Then, the numerical results were compared with the results predicted by the ANN model, which showed a complete agreement with the numerical results. In addition, the ANN model was trained by excluding the data points used in an experiment [44]. The results showed how well the model is capable of predicting the experimental results, too.

## NOMENCLATURE

$A_c$ : area of fraction of the heater surface subjected to convection [$m^2$]

$A_q$ : area of fraction of the heater surface subjected to quenching [$m^2$]

$C_p$ : specific heat of the fluid [J kg$^{-1}$ K$^{-1}$]
$d_w$ : bubble departure diameter on the wall [m]
$F_{lg}$ : action of interfacial forces from vapor on liquid [N]
$F_{gl}$ : action of interfacial forces from liquid on vapor [N]
f : bubble departure frequency [Hz]
$\alpha$ : volume fraction
$S_i$ : additional source terms due to coalescence and breakage [kg m$^{-3}$ s$^{-1}$]
$f_i$ : scalar fraction related to the number density of the discrete bubble classes
G : mass flux [kg m$^{-2}$ s$^{-1}$]
g : gravitational constant [m s$^{-2}$]
H : specific enthalpy [J kg$^{-1}$]
h : interfacial heat transfer coefficient [J kg$^{-1}$]
$h_{fg}$ : specific latent heat of vaporization [J kg$^{-1}$]
k : conductivity [W m$^{-2}$ K$^{-1}$]
m : mass [kg]
$\dot{m}$ : mass flux [kg m$^{-2}$ s$^{-1}$]
$n_a$ : active nucleation site density [m$^2$]
n : number of data points
P : pressure [N m$^{-2}$]
$q_c$ : heat transfer due to forced convective [W m$^{-2}$]
$q_e$ : heat transfer due to evaporation [W m$^{-2}$]
$q_q$ : heat transfer due to quenching [W m$^{-2}$]
q : heat flux [W m$^{-2}$]
$R^2$ : R_squared
St : stanton number [St=h/$\rho$uc$_p$]
T : temperature [K]
$T_{sup}$ : wall superheat temperature [K]=$T_w - T_{sat}$
$T_{sub}$ : subcooled temperature [K]
$T_w$ : wall temperature [K]
$t_w$ : bubble detachment waiting time [s]
t : time [s]
u : velocity [m s$^{-1}$]
$X_{in}$ : entrance length [m]
$Y_i$ : real value of the target quantity
$\hat{Y}_i$ : predicted value of the target quantity by the ANN
$\overline{Y}$ : mean of the data

**Greek Letters**

$\mu$ : viscosity [Pa·s]
$\rho$ : density [kg m$^{-3}$]
$\sigma$ : surface tension [N m$^{-1}$]
$\Gamma_{lg}$ : interfacial mass transfer from vapor to liquid [kg m$^{-3}$ s$^{-1}$]
$\Gamma_{gl}$ : interfacial mass transfer from liquid to vapor [kg m$^{-3}$ s$^{-1}$]

**Subscripts**

g : vapor
*l* : liquid
w : wall

**Superscripts**

e : Euler's number

**Abbreviations**

ANN : artificial neural network
HTC : heat transfer coefficient

## REFERENCES


1. Y. Qiu, D. Garg, L. Zhou, C. R. Kharangate, S.-M. Kim and I. Mudawar, *Int. J. Heat Mass Transfer*, **149**, 119211 (2020).
2. G. P. Celata, M. Cumo, A. Mariani and G. Zummo, *Int. J. Therm. Sci.*, **39**(9-11), 896 (2000).
3. Z. Guo, J. Yang, Z. Tan, X. Tian and Q. Wang, *Int. J. Heat Mass Transfer*, **174**, 121296 (2021).
4. J. Zhou, J. Bai and Y. Liu, *Micromachines*, **13**(5), 781 (2022).
5. J. Lee, D. Jo, H. Chae, S. H. Chang, Y. H. Jeong and J. J. Jeong, *Exp. Therm. Fluid Sci.*, **69**, 86 (2015).
6. Q. Fan, Z. Zhang and X. Huang, *Adv. Theory Simulations*, 2200047 (2022).
7. G. Zhang, J. Chen, Z. Zhang, M. Sun, Y. Yu, J. Wang and S. Cai, *Smart Mater. Struct.*, **31**(7), 075008 (2022).
8. M. E. Steinke and S. G. Kandlikar, *J. Heat Transfer*, **126**(4), 518 (2004).
9. D. Jige and N. Inoue, *Int. J. Heat Fluid Flow*, **78**, 108433 (2019).
10. V. Schrock and L. Grossman, *Forced convection boiling studies. final report on forced convection vaporization project*, California. Univ., Berkeley. Inst. of Engineering Research (1959).
11. J. Bennett, *Trans. Inst. Chem. Eng.*, **39**, 113 (1961).
12. J. C. Chen, *Ind. Eng. Chem. Process Des. Dev.*, **5**(3), 322 (1966).
13. M. M. Shah, *ASHRAE Trans.; (United States)*, **88**, 185 (1982).
14. D. L. Bennett and J. C. Chen, *AIChE J.*, **26**(3), 454 (1980).
15. S. G. Kandlikar, *J. Heat Transfer*, **112**(1), 219 (1990).
16. H. J. Lee and S. Y. Lee, *Int. J. Multiphase Flow*, **27**(12), 2043 (2001).
17. H. Alimoradi, S. Zaboli and M. Shams, *Korean J. Chem. Eng.*, **39**(1), 69 (2022).
18. S. Zaboli, H. Alimoradi and M. Shams, *J. Therm. Anal. Calorim.*, **147**, 10659 (2022).
19. S. S. Bertsch, E. A. Groll and S. V. Garimella, *Int. J. Heat Mass Transfer*, **52**(7-8), 2110 (2009).
20. D. L. Bennett, M. W. Davies and B. L. Hertzler, *Am. Inst. Chem. Eng. Symposium Ser.*, **76**, 91 (1980).
21. S. Edelstein, A. Perez and J. Chen, *AIChE J.*, **30**(5), 840 (1984).
22. X. Fang, Q. Wu and Y. Yuan, *Int. J. Heat Mass Transfer*, **107**, 972 (2017).
23. M. Piasecka, *Int. J. Heat Mass Transfer*, **81**, 114 (2015).
24. K. Strąk and M. Piasecka, *Int. J. Heat Mass Transfer*, **158**, 119933 (2020).
25. S. Paul, M. Fernandino and C. A. Dorao, *Int. J. Heat Mass Transfer*, **164**, 120589 (2021).
26. G. Zhang, Z. Zhang, M. Sun, Y. Yu, J. Wang and S. Cai, *Adv. Eng. Mater.*, 2101680 (2022).
27. B. Chen, Y. Lu, W. Li, X. Dai, X. Hua, J. Xu, Z. Wang, C. Zhang, D. Gao and Y. Li, *Int. J. Heat Mass Transfer*, **192**, 122927 (2022).
28. M. Ahmadlou, M. R. Delavar, A. Basiri and M. Karimi, *J. Indian Soc. Remote Sensing*, **47**(1), 53 (2019).
29. H. A. Amirkolaee, H. Arefi, M. Ahmadlou and V. Raikwar, *Remote Sensing Environ.*, **274**, 113014 (2022).
30. A. Azadeh, M. Saberi, A. Kazem, V. Ebrahimipour, A. Nourmohammadzadeh and Z. Saberi, *Appl. Soft Comput.*, **13**(3), 1478 (2013).
31. L. Zhou, Q. Fan, X. Huang and Y. Liu, *Optimization*, In press

(2022).
32. H. Alimoradi and M. Shams, *Appl. Therm. Eng.*, **111**, 1039 (2017).
33. Y. Seong, C. Park, J. Choi and I. Jang, *Energies*, **13**(4), 968 (2020).
34. X. Wang and X. Lyu, *Ocean Eng.*, **221**, 108508 (2021).
35. Y. Wang, H. Wang, B. Zhou and H. Fu, *Ocean Eng.*, **242**, 110106 (2021).
36. S. Cheung, S. Vahaji, G. Yeoh and J. Tu, *Int. J. Heat Mass Transfer*, **75**, 736 (2014).
37. B. E. Launder and D. B. Spalding, *Comput. Meth. Appl. Mech. Eng.*, **3**, 269 (1974).
38. W. E Ranz and W. R. Marshall, *Chem. Eng. Prog.*, **48**(3), 141 (1952).
39. M. Ishii and N. Zuber, *AIChE J.*, **25**(5), 843 (1979).
40. N. Kurul and M. Z. Podowski, *Multidimensional effects in forced convection subcooled boiling*, In: Proceedings of the 9th Heat Transfer Conference, 19-24 (1990).
41. M. Lemmert and J. M. Chawla, *Influence of flow velocity on surface boiling heat transfer coefficient*, In: Boiling, Hahne, E., Grigull, U. (Eds.), Heat Transfer. Academic Press and Hemisphere, ISBN 0-12-314450-7, pp. 237-247 (1977).
42. V. I. Tolubinsky and D. M. Kostanchuk, Vapour bubbles groth rate and heat transfer intensity at subcooled water boiling; Heat Transfer 1970, Preprints of papers presented at the 4th International Heat Transfer Conference, vol. 5, Paris (Paper No. B-2.8) (1970).
43. R. Cole, *AIChE J.*, **6**(4), 533 (1960).
44. G. Bartolomei, V. Brantov, Y. S. Molochnikov, Y. V. Kharitonov, V. Solodkii, G. Batashova and V. Mikhailov, *Therm. Eng.*, **29**(3), 132 (1982).
45. S. Z. Rouhani and E. Axelsson, *Int. J. Heat Mass Transfer*, **13**(2), 383 (1970).
46. A. Krizhevsky, I. Sutskever and G. E. Hinton, *Commun. ACM*, **60**(6), 84 (2017).
47. D. Svozil, V. Kvasnicka and J. Pospichal, *Chemom. Intell. Lab. Syst.*, **39**(1), 43 (1997).
48. D. P. Kingma and B. Jimmy, *Adam: A method for stochastic optimization*, arXiv preprint arXiv:1412.6980 (2014).
49. A. E. Bergles and W. M. Rohsenow, *ASME J. Heat Transfer*, **1**, 365 (1964).
50. D. Liu, P.-S. Lee and S. V. Garimella, *Int. J. Heat Mass Transfer*, **48**(25-26), 5134 (2005).
51. N. Basu, G. R. Warrier and V.K. Dhir, *J. Heat Transfer*, **124**(4), 717 (2002).
52. G. Costigan and P. Whalley, *Int. J. Multiphase Flow*, **23**(2), 263 (1997).
53. N. Basu, G. R. Warrier and V. K. Dhir, *J. Heat Transfer*, **127**(2), 131 (2005).
54. W. Friz, *Physic. Zeitschz.*, **36**, 379 (1935).
55. L. Yang, A. Guo and D. Liu, *Exp. Heat Transfer*, **29**(2), 221 (2016).
56. R. Sugrue, J. Buongiorno and T. McKrell, *Nucl. Eng. Des.*, **279**, 182 (2014).
57. J. Yoo, C. E. Estrada-Perez and Y. A. Hassan, *Int. J. Multiphase Flow*, **84**, 292 (2016).
58. C.-Y. Han and P. Griffith, *Int. J. Heat Mass Transfer*, **8**, 905 (1965).
59. L. Z. Zeng and J. F. Klausner, *J. Heat Transfer*, **115**, 215 (1993).